scientific reports

OPEN

A quantitative characterization of the heterogeneous response of glioblastoma U-87 MG cell line to temozolomide

Pragyesh Dixit[1], Ilyas Djafer-Cherif[1], Saumil Shah[2], Karolina Drabik[1], Arne Traulsen[2] & Bartlomiej Waclaw[1,3✉]

Most cancers are genetically and phenotypically heterogeneous. This includes subpopulations of cells with different levels of sensitivity to chemotherapy, which may lead to treatment failure as the more resistant cells can survive drug treatment and continue to proliferate. While the genetic basis of resistance to many drugs is relatively well characterised, non-genetic factors are much less understood. Here we investigate the role of non-genetic, phenotypic heterogeneity in the response of glioblastoma cancer cells to the drug temozolomide (TMZ) often used to treat this type of cancer. Using a combination of live imaging, machine-learning image analysis and agent-based modelling, we show that even if all cells share the same genetic background, individual cells respond differently to TMZ. We quantitatively characterise this response by measuring the doubling time, lifespan, cell cycle phase, area and motility of cells, and determine how these quantities correlate with each other as well as between the mother and daughter cell. We also show that these responses do not correlate with the cellular level of the enzyme MGMT which has been implicated in the response to TMZ.

Cancer is a disease in which genetic or epigenetic alterations cause cells to proliferate in an uncontrolled way. While many cancers can be attributed to extrinsic factors (smoking, radiation, exposure to UV), more than half are thought to be "bad luck" caused by errors during DNA replication[1,2].

One of the most common modes of cancer treatment, alongside surgery and radiotherapy, is chemotherapy. Traditional (non-targeted) cytotoxic chemotherapy works because cancer cells have a different proliferation or drug uptake rate compared to normal cells, and are thus more susceptible to the drug[3]. By carefully adjusting the drug dose, cancer cells can be eliminated while minimising the effect on healthy cells. However, the difference between a dose toxic to cancer cells and a dose toxic to normal cells is often small, and even a minor increase in the resistance of cancer cells or the existence of a slightly more resistant subpopulation can lead to treatment failure. Resistance to anticancer drugs can come about in different ways[4] such as genetic mutations which lead to decreased drug uptake, increased drug efflux, changes in metabolism, or cell death inhibition[5]. Resistance can also be caused by tumour microenvironment – a complex network of interactions between cancer cells and the surrounding normal tissue[6–8]. All these mechanisms can lead to substantial heterogeneity in the response of different cells within the tumour to chemotherapy.

Although we now have a very good understanding of genetic heterogeneity in cancer[9–15], this is not paralleled by the understanding of non-genetic mechanisms that cause diverse phenotypic responses to drugs. In general, many different mechanisms can cause phenotypic diversity in eukaryotic cells. Two of them, stochasticity in gene expression[16] and epigenetic regulation via chromatin modifications[17], are particularly well established. However, their effect on cancer chemotherapy is not entirely clear.

Phenotypic diversity and its relationship to therapeutic response has been investigated in glioblastoma multiforme (GBM), an aggressive brain cancer. GBM is usually treated with surgery, followed by adjuvant radio- and/or chemotherapy. Chemotherapy typically involves alkylating agents such as temozolomide (TMZ) or carmustine (also called BCNU). In particular, TMZ adds methyl groups to guanine in the DNA; an attempt

[1]Dioscuri Centre for Physics and Chemistry of Bacteria, Institute of Physical Chemistry, Polish Academy of Sciences, Kasprzaka 44/52, Warszawa 01-224, Poland. [2]Department of Theoretical Biology, Max Planck Institute for Evolutionary Biology, Plön, Germany. [3]School of Physics and Astronomy, The University of Edinburgh, JCMB, Peter Guthrie Tait Road, Edinburgh EH9 3FD, UK. ✉email: bwaclaw@ichf.edu.pl

by the cell to repair damaged base pairs sometimes leads to DNA double-strand breaks occurring during cell replication. A large number of methyl adducts thus leads to DNA fragmentation and cell death[18]. However, cells express the enzyme MGMT (O-6-methylguanine-DNA methyltransferase) which removes methyl groups from guanine[19]. Early studies demonstrated that MGMT promoter CpG methylation (natural regulatory mechanism, different to TMZ- induced methylation), which reduces the expression of MGMT, correlates with better treatment outcome in TMZ chemotherapy[20]. Indeed, MGMT promoter methylation predicts TMZ sensitivity in in vitro clonogenic assays[21]. However, it seems that MGMT promoter methylation is not the only factor; the authors of[22] have shown that while there is heterogeneity in MGMT promoter methylation in tumours, it does not fully correlate with MGMT expression. They have also detected genetic mutations in other pathways implicated in resistance to TMZ. A recent analysis of single cells harvested from GBM tumours showed the presence of many genetic and epigenetic alterations, and demonstrated that individual clones responded differently to TMZ, which could at least partially be explained by epigenetic alterations in regulatory regions of relevant genes[23].

In this work, we characterise the response of single glioblastoma cells to TMZ. We culture the cells in vitro, expose them to TMZ, and optically monitor their behaviour. Taking the advantage of machine-learning approaches to phenotyping[24,] we track individual cells and perform quantitative analysis of their behaviour. We confirm that there is significant heterogeneity in cell phenotype (division rate, motility, death rate). We then investigate the hypothesis that phenotypic, non-genetic heterogeneity in MGMT expression can cause different cells to respond differently to TMZ. Using a fluorescently-tagged MGMT, we show that there is no correlation between the intracellular concentration of MGMT and cell fate. We conclude that other mechanisms that do not involve MGMT may be more relevant for the observed diversity in the sensitivity of genetically-identical glioblastoma cells to TMZ.

Results

To investigate the response of glioblastoma cells to temozolomide (TMZ), we used the U-87 MG cell line[25]. We first performed a clonogenic assay to select an appropriate range of TMZ concentrations for subsequent live-imaging experiments (SI Fig. S1A). The assay showed that the proportion of cells surviving TMZ treatment was close to zero for 500 µM TMZ whereas 10 µM was sufficient to cause a detectable reduction in proliferation. Based on this result, we selected 0, 10, and 500 µM TMZ as the control, low, and high TMZ concentrations. For reference, 10 µM is typical and 50 µM is at the upper end of what has been measured in vivo following TMZ chemotherapy, but some in vitro studies use concentrations higher than 500 µM[26,27].

The design of live-imaging experiments is schematically shown in Fig. 1A. We seeded U-87 MG cells in a 24-well plate. After an initial incubation period (16 h), we replaced the cell culture medium with the same medium containing different concentrations of TMZ (0, 10 or 500 µM), and imaged the cells for up to 150 h using a wide-field epi-fluorescent microscope. We then used machine-learning image segmentation to count the number of cells $N(t)$ at each time point t. Figure 1B shows the fold-change $N(t)/N(0)$ ($t = 0$ h corresponding to when TMZ was added) for the control (DMSO without TMZ) and TMZ-treated populations. The control population continues to grow at all times. In contrast, growth slows down in TMZ-treated populations and eventually approaches zero net growth for 500 µM TMZ.

The cells showed a delayed response to TMZ. Although this has been anticipated based on the known mechanism of action of TMZ[28], the response was somewhat faster than expected. Previous research[29] suggested that TMZ should lead to cell death during the 2nd replication cycle since the TMZ exposure. We observed reduced growth after less than one doubling time (Fig. 1B), which may confirm recent suggestions[30] that DNA
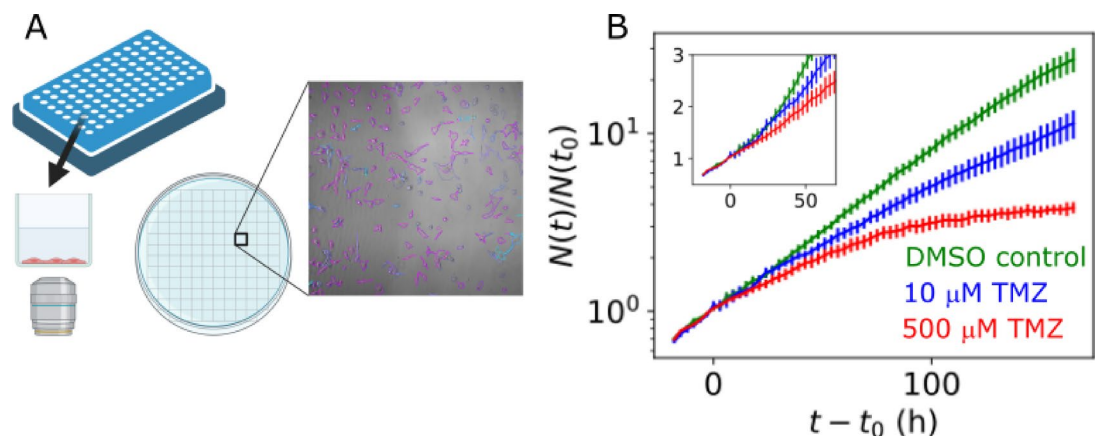

Fig. 1. (**A**) Schematic of the live-imaging experiment. Cells are incubated in the wells of a 24-well plate and imaged through the bottom. Multiple fields of view (FOV) are acquired to cover a large fraction of each well. Imaged cells are detected using a machine-learning segmentation algorithm. (**B**) Growth curves (fold change as a function of time) of U-87 MG treated with different concentrations of TMZ. The exponential growth rate of the control population is 0.02 h^{-1}, which corresponds to the population doubling time 35 ± 1 h. The inset shows a zoomed-in version of the same plot, in linear scale. All curves represent averages of $n = 3$ replicates, error bars = standard error of mean (SEM).

methylation is not the only mechanism of TMZ-induced cytotoxicity, or that other forms of DNA damage manifest much earlier through, e.g., cell cycle arrest.

A reduction in the growth rate was also observed if TMZ-containing medium was replaced with no-drug medium after 2 h (SI Fig. S1C), whereas a slightly weaker but very similar response was induced by treating cells with TMZ for only 30 min (SI Fig. S1D). This is consistent with the drug half-life of about 2 h[31], hence the effective exposure time to TMZ is very short even if the drug is not replaced by the drug-free medium. Curiously, the response seen in SI Fig. S1C is stronger than that in Fig. 1B – we attribute this to slightly different experimental conditions (see Materials and Methods and the caption of Fig. S1C).

To elucidate the effect of TMZ on individual cells, we tracked the cells and reconstructed cell relatedness from the tracking data (Fig. 2A). Figure 2BC shows the per-cell birth and the death rate as a function of time, for the control and 500 μM TMZ populations. In agreement with population-wide results, we observe that cells continue to divide in the control population; the average birth rate is about 0.035 h^{-1}, and the death rate is about 0.003 h^{-1} initially, and increases to about 0.013 h^{-1} towards the end of the experiment. The difference between the birth and death rates is very close to the exponential growth rate 0.02 h^{-1} from Fig. 1B. The TMZ-treated cells replicate initially with the same rate as the control cells, but growth slows down significantly after the first 24 h. Figure 2C shows that the death rate is only slightly larger in the treated versus the control population, therefore the reduction in growth observed in Fig. 1B is predominantly caused by reduced replication (Fig. 2B) rather than increased death. This shows that TMZ is mostly cytostatic[32] during the first days of treatment. However, as the two-week long clonogenic assay shows (SI Fig. S1A), high TMZ concentrations eventually lead to cell death; this is not visible in Fig. 2C due to the increasing cell density making cell tracking difficult after four days. However, Fig. 1B suggests that cytostatic effects of a single dose of TMZ continue for at least 6 days.

We also determined cell trajectory lifespan, defined as the time since cell's birth to either death, division, or the end of the experiment, whichever comes first. Figure 2D shows that untreated cells have shorter trajectory lifespans compared to treated cells. However, branch length, defined as time between two divisions, shows no difference between control and treated cells (Fig. 2E). This could indicate that those cells which continued to divide, behaved similarly in both conditions.

Next, we determined the motility of treated and control cells. Figure 3A shows that the average speed, with which cells in the control population moved, slowly increased over time. However, the average speed of cells
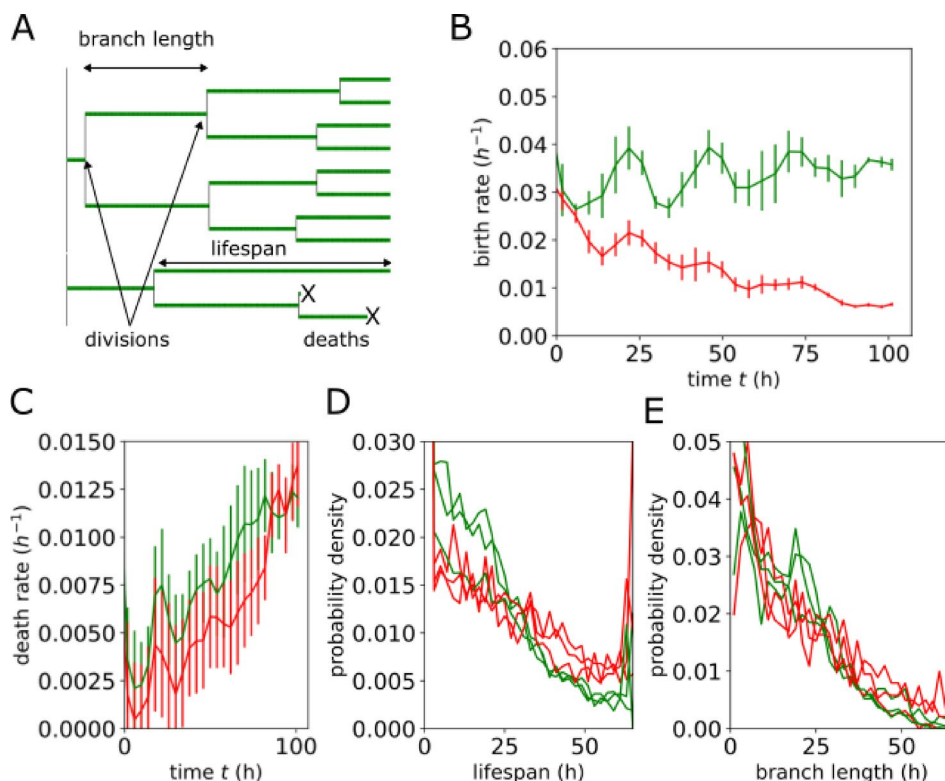

Fig. 2. (**A**) Example of a lineage tree from the control experiment. Arrows indicate two selected divisions and "x" mark two death events; the doubling time ("branch length") is the period of time between two divisions along a single branch of the tree. (**B, C**) Birth and death rates versus time ($n = 3$ replicates), obtained from the number of observed birth and death events as $N_{\text{events}}(t) / (\Delta t\, N_{\text{cells}}(t))$ where Δt is the time interval in which the events occurred. In each replicate, between 350 and 1000 births were manually tracked. (**D**) Probability distribution of trajectory lifespan for the control (green) and 500 μM TMZ (red). (**E**) Probability distribution of branch length in the lineage tree ("cell doubling time"). In panels (**D, E**) each curve is an individual replicate ($n = 3$) with between 2.5k and 11k trajectories analysed.
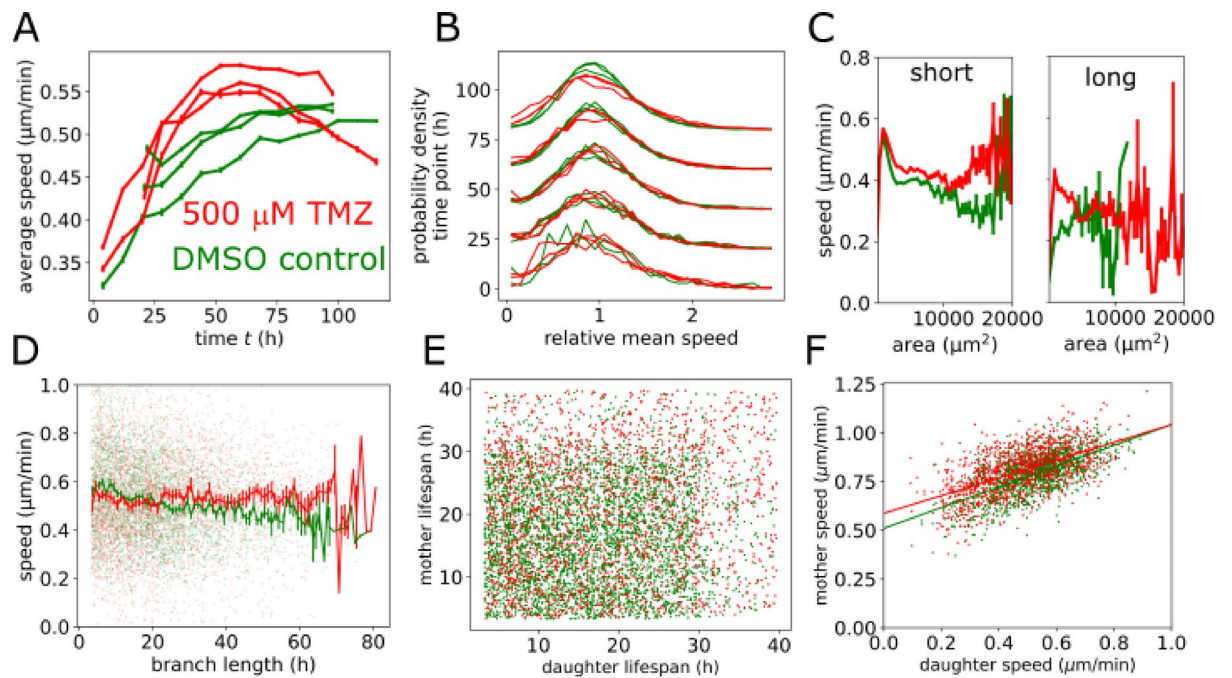
Fig. 3. (**A**) Mean speed (averaged over all tracked cells) as a function of time, for the control and 500 μM TMZ population. (**B**) Probability distributions of finding a cell with a given speed relative to the mean speed at that time point, in the control and treated populations, for different times. Between 3.5k and 20k trajectories have been analysed. (**C**) Speed versus cell size for short ($t < 33\,h$) and long ($t > 66\,h$) branches. Long branches represent cells with cell cycle arrest. (**D**) Average speed versus branch length (inter-division time), for individual cellular trajectories (points). Lines represent mean values of the distributions. (**E**) Mother and daughter cells' trajectory lifespans. (**F**) Correlation between the mother and daughter average velocities. Points represent individual cells; lines are linear fits. In all plots, green = control, red = 500 μM TMZ, and $n = 3$ replicates have been analysed. Errors = SEM.

treated with 500 μM TMZ initially increased faster and then started to slowly decrease towards the end of the experiment (Fig. 3A). In the mid-phase of the experiment ($t = 40 - 60\,h$), TMZ-treated cells were more motile than cells in the control population. Figure 3B shows the distribution of cell velocities divided by the mean velocity, from the control and 500 μM TMZ populations; the distributions are very similar. This could mean that treatment increases the motility of each cell by a similar factor as opposed to, e.g., making only a fraction of the population more motile, which would change the shape of the distribution. A small but statistically significant difference visible at later times ($p_{\text{value}} < 0.001$ for $t = 60 - 80\,h$) could mean that, eventually, cells destined for survival or death have slightly different motilities but this effect shows up only for much longer trajectories than sampled in our experiments.

Interestingly, there is a difference in motility between treated and non-treated cells that do not divide for at least 2 average doubling times (Fig. 3C). Moreover, motility correlates with cell area differently for control (positive correlation) than treated (negative correlation) cells. Treated and non-treated cells with short branches (division events separated by less than one average doubling time) do not show this reciprocal correlation, except for the largest cells (Fig. 3C).

Those cells that continued to divide showed a small negative correlation between branch length (time between divisions) and motility in the control population (Pearson's $r = -0.19$) but no correlation in the treated population (Fig. 3D)); the two populations were statistically different (2D KS test $p_{\text{value}} < 10^{-6}$). The lack of strong proliferation-motility correlation is interesting, as previous research suggested a trade-off between proliferation and motility, i.e. faster-moving cells would be expected to divide less often than slowly-moving cells, or that some sort of division of labour should exist in the population of cancer cells[33–35]. Although we found evidence for a small potential trade-off in the control experiment, this effect was absent in treated cells. Since Fig. 3D shows only proliferating cells and the control and treated populations have a similar distribution of division rates and velocities, this suggests that treated and non-treated subpopulations of proliferating cells share a similar phenotype. This could mean that cells have different sensitivity to TMZ, and treatment selects a subpopulation of cells (which continue to divide) that are less sensitive.

There is no correlation between the trajectory lifespan of mother and daughter cells (Fig. 3E), but we have found a statistically significant correlation between the motility of mother and daughter cells in the control population (Fig. 3F, $R = 0.64$; $p_{\text{value}} < 10^{-12}$), which suggests that cell phenotype is heritable to some extent. A similar but slightly weaker correlation is visible for TMZ treated cells (Fig. 3F, $R = 0.58$, $p_{\text{value}} < 10^{-12}$).

These results suggest heritable phenotypic heterogeneity in U-87 MG cells undergoing TMZ treatment. Since, as we indicated in the introduction, MGMT has been implicated in resistance to TMZ, we hypothesised that intracellular variations of MGMT may be responsible for the observed heterogeneous response to TMZ.

To further quantify this heterogeneity, we classified cellular trajectories into short (duration < 33 h, approx. 1 average doubling time in the control experiment) and long (duration > 66 h, approx. two doubling times). We obtained that, in the control population, $91 \pm 1\%$ and $1 \pm 0.3\%$ of cells had short/long trajectories, whereas in the TMZ-treated population the proportions were $76 \pm 3\%$ and $3 \pm 1\%$, respectively. Therefore, TMZ treatment increased the fraction of slowly-dividing or arrested cells.

We also plotted cell area versus time for single-cell trajectories (SI Fig. S2BC). These trajectories clearly show strong population heterogeneity, both in the control and treated populations.

To gain a better insight into how TMZ was affecting proliferation and death, we used the FUCCI system[36] to determine the position of each cell in the cell cycle, and correlated this with cell fate (Fig. 4). We observed that, while control cells that successfully divided typically went through a single phase of the cell cycle, treated cells often attempted to divide, but failed to separate after the end of the G2 phase (Fig. 4CE). Cells that failed to divide showed much slower oscillations of the FUCCI reporters (CDT1 and Geminin). The comparable intensity of the two signals, in particular at the end of the trajectory, suggests cell cycle arrest at the end of the G1 phase.

To see if varying the intracellular concentration of MGMT affected the response of individual cells to TMZ, U-87 MG cells (approx. 2500/well) were seeded in a 24-well plate and transfected with a plasmid containing a fluorescently tagged MGMT. We imaged the cells for 48 h until some of them started showing bright fluorescence in the nucleus (MGMT exhibits nuclear localization, SI Fig. S3), and then replaced the medium with a fresh growth medium supplemented with 500 μM TMZ. We continued imaging the cells for another $\sim$ 70 h, tracked individual cells and, using automated image analysis, calculated the total fluorescence in each cell (a proxy for intracellular MGMT concentration). The drawbacks of this approach were (i) not accounting for endogenous, untagged MGMT, (ii) much higher levels of tagged MGMT compared to the WT cells, (iii) MGMT concentration varying in time. However, since MGMT expression was significantly enhanced in this cell line, we reasoned that any effect of MGMT heterogeneous expression on cell fate should be easy to detect, thus providing a simple test of our hypothesis that MGMT and cell fate are correlated.

Figure 5AB shows trajectory lifespan (defined above) and motility versus the time-averaged fluorescence of MGMT-C-GFPspark in single cells. We see that, despite a very significant (three orders of magnitude) difference in fluorescence, there is no correlation between motility and fluorescence (control $p_{\mathrm{value}} = 0.32$, treated $p_{\mathrm{value}} = 0.91$), but there is a small correlation between lifespan and fluorescence (control $p_{\mathrm{value}} = 0.003$, treated $p_{\mathrm{value}} = 0.01$). However, this correlation is present in both control and treated cells, and the two data sets are statistically the same ($p_{\mathrm{value}} = 0.06$). This suggests that the correlation is not caused by treatment. A possible explanation is that cells that live longer accumulate more MGMT, so the causation is opposite to what we would expect based on our hypothesis. This means that, at least for the specific cell line used here (U-87 MG), MGMT does not seem to contribute towards resistance against TMZ during the first 72 h post-TMZ exposure.

Mathematical model provides insight into the mechanism of TMZ action

To further confirm our understanding of the population dynamics of TMZ-treated cells, we have developed a simple agent-based model that can reproduce the population-level response from Fig. 1B. The model assumes that TMZ methylates some vital components of the cell; the model is agnostic to whether this is DNA or some other molecules such as RNA, histones, or other proteins. Each cell in the model is a separate object with its own internal state, describing the current phase in the cell cycle and whether TMZ-induced methylation has already occurred or not. The cell cycle is divided into three phases; their lengths T_1, T_2, T_3 are the parameters of the model. Cells are methylated only during the second phase with rate r_{drug} which depends on the dose of TMZ; $r_{\mathrm{drug}} = 0$ when simulating the control experiment. Cells replicate (if not methylated) or die (if methylated) at the end of the cycle. Figure 6A shows the main steps of the computer algorithm used to simulate the model.

The model fits the data reasonably well (Fig. 6B). Best-fit parameters are: cell cycle duration $T = 33$ h, methylation starting at the beginning of the cell cycle, $T_1 = 1.5$ h, $T_2 = 0.5$ h, and methylation rate $r_{\mathrm{drug}} = 1.025$ h^{-1} (500 μM TMZ) and 0.582 h^{-1} (10 μM TMZ). This gives us a potentially interesting insight into the mechanism of action of TMZ. Since the model does not assume that cell death must occur in the 2nd round of replication due to irreparable double-stranded DNA breaks (DSBs) as suggested by earlier works, but it may occur already during the 1st replication round, the agreement between the model and the experimental data supports the idea that TMZ-induced DNA methylation causes cell cycle arrest/cell death even before damaged basepairs are converted into DSBs, or that TMZ has also non-DNA targets. The latter also agrees with the observed lack of correlation between MGMT level and cell fate, because MGMT is not expected to remove methyl adducts other than those on the DNA. Indeed, there is already evidence[30,37] that TMZ may have cellular targets other than the DNA.

Conclusion

In this work we have investigated how glioblastoma multiforme cancer cells respond to in vitro chemotherapy with temozolomide (TMZ). We cultured a population of U-87 MG cells in multi-well plates, exposed them to TMZ and imaged for several days using an automated microscope. We observed a heterogeneous response to TMZ, i.e., some cells continued to replicate whereas others stopped growing or even died. After some time, growth practically ceased but most surviving cells remained motile. Treated cells also become more motile than the untreated control population. Cells that kept dividing exhibited correlations between the phenotype of the mother and daughter cell (similar motility). This complements earlier work on the motility of different GBM cell lines in the absence of therapy[38] or during targeted therapy[39].
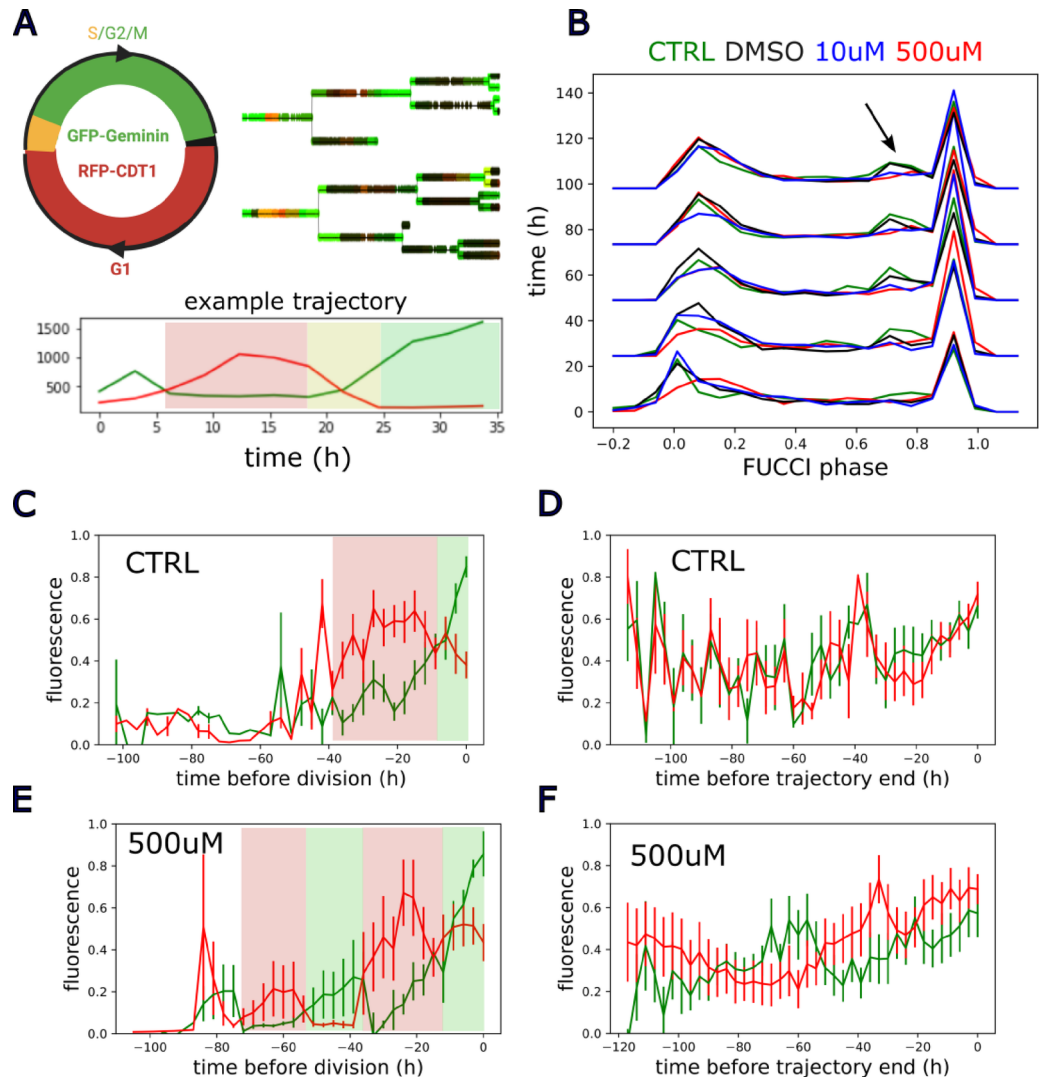
Fig. 4. Cell-cycle fluorescence reporter system FUCCI shows failed replication cycles in TMZ-treated cells. (**A**) FUCCI uses two fluorescent proteins (green and red) to indicate the position in the cell cycle. Two lineage trees from the control experiment show how the fluorescence signal changes along each branch. A plot below shows an example of the red $R(t)$ and green $G(t)$ fluorescence for a cell that successfully divided at $t = 35$ h. (**B**) Histograms of the "cell cycle phase" φ calculated as $\varphi = G(t)/(G(t) + R(t))$. Between 0.5k and 4.3k cells have been analysed. A peak close to zero represents cells in the G1 phase, whereas a peak close to 1 represents cells in the G2/M phase. As time progresses, the control population develops a third, smaller peak close to $\varphi \approx 0.7$ (arrow), whereas treated cells do not exhibit this peak. (**C**-**F**) Average red and green fluorescence along trajectories that end up with a division (panels **C**, **E**) or cell death/detachment (panels **D**, **F**), for the control and 500 µM TMZ. The time before division is calculated as $t - t_0$, where t is the time at which fluorescence was obtained and t_0 is the time of division ($t_0 > t$), hence the negative values on the horizontal axis. Shaded areas indicate G1 and G2/M phases. The plot for treated cells that went on to divide shows the evidence of failed earlier divisions. In treated cells that did not divide, FUCCI signals vary much more slowly, indicating a possible cell cycle arrest. A single biological replicate has been analysed and only human-verified trajectories have been included ($n = 28, 35, 14, 10$, respectively). Errors = SEM.

Treated cells slowed down replication after less than a single doubling of the control population. This response was faster than expected based on the suggested mechanism of action of TMZ: DNA methylation followed by failed repair before the first cell division, followed by double-strand breaks and death during the second round of replication.

We also performed an experiment in which cells were transfected with a plasmid containing a fluorescently-tagged MGMT protein. The protein was expressed to very different levels in different cells (fluorescence varying by three orders of magnitude) and exhibited nuclear localization typical of the native MGMT. However, we could not find any correlation between the phenotype (motility, doubling time, cell fate) and fluorescence that could be attributed to the action of TMZ.
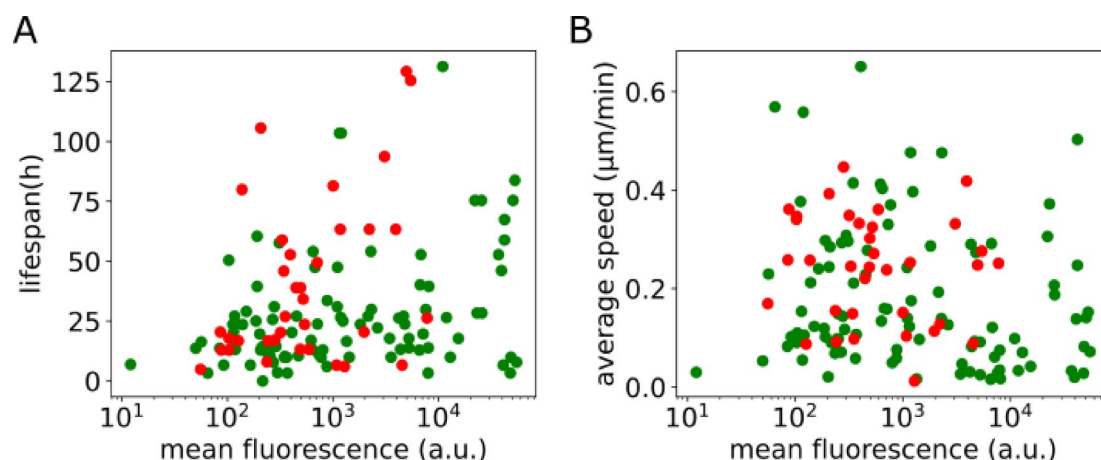
Fig. 5. (**A**) Trajectory lifespan versus mean fluorescence of MGMT-C-GFPspark, for single cells from the control (green) and treated (red) populations. (**B**) As in (**A**) but for mean speed versus mean fluorescence. Data points come from two replicate experiments (control) and a single replicate (treated cells).
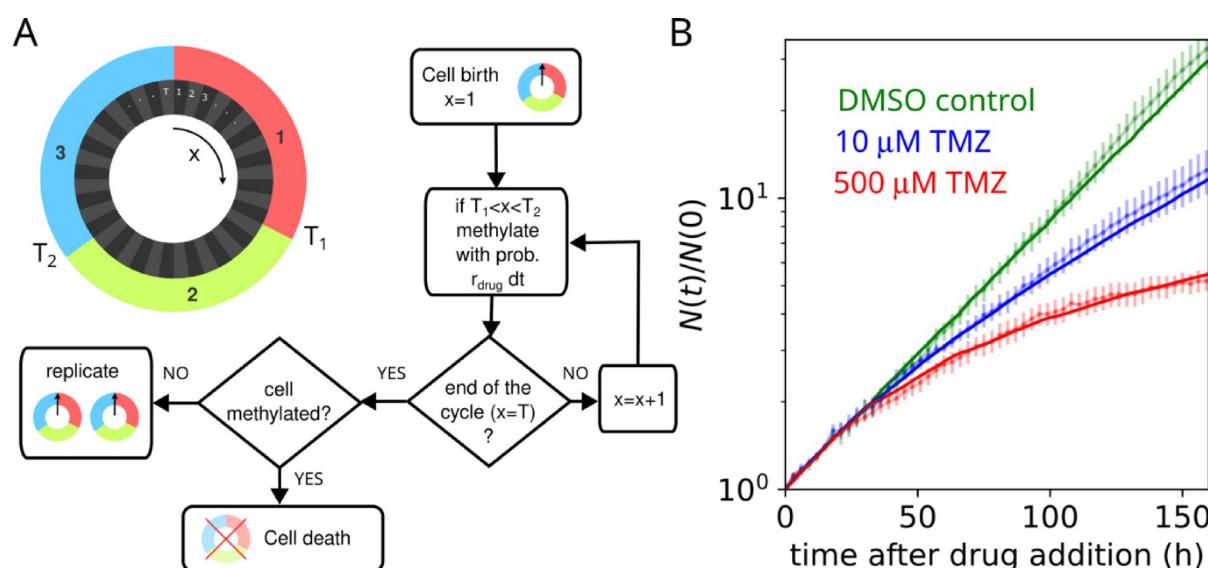

Fig. 6. (**A**) A schematic of the computer algorithm used to simulate the mathematical model. (**B**) Experimental growth curves (fold-change versus time) compared to the prediction of the model. Points = experimental growth curves from Fig. 1, lines = computer model (average of 4 replicates per condition).

This, together with the observation that the response to TMZ is faster than expected based on DNA damage-induced cell death, suggests that there must be other mechanisms of action of TMZ that either do not rely on DSBs causing cell death, or do not involve DNA damage at all. This also means that protection against TMZ does not rely on MGMT alone. For example, an important protection mechanism against DNA damage is the base excision repair system (BER), which removes other types of DNA methyl adducts that MGMT cannot handle[40]. Although cell-to-cell variations in the strength of BER response could be responsible for the observed heterogeneous response to TMZ, there is evidence that in U-87 MG cells treated with TMZ, growth arrest is independent of BER[41]. Other, non-DNA damage mechanisms may therefore be at play here.

Our conclusions are further supported by a mathematical model, which shows that early damage induced by TMZ is sufficient to explain the observed growth curves of control and treated cells.

Our research has several potential shortcomings that could be rectified in future studies:

- No information about the level of endogenous MGMT: we did not fluorescently tag the endogenous MGMT and hence could not determine how diverse its expression was among the cells. However, MGMT expression in U-87 MG is supposedly low[42]. Moreover, the overexpression experiment did not show any correlation between fluorescently tagged MGMT and the response to TMZ. We would therefore not expect endogenous

MGMT to behave differently. This may be different in other cell lines or different concentrations/dosage of TMZ.
- Treatment too short to observe long-term TMZ effects: while the clonogenic assay showed no surviving clones at 500 μM TMZ, only a small fraction of cells died 72 h post-TMZ in live-cell imaging experiments. Longer experiments could be possible but they would be challenging due to the medium being used up, evaporation, and cell crowding.

Regarding the observed lack of correlation between MGMT and the TMZ-induced phenotype, we identified the following potential problems:

- MGMT-C-GFPspark protein may not be active due to misfolding caused by the fluorescent tag. We did not test the enzymatic activity of tagged MGMT. However, others have shown that a similarly fluorescently tagged MGMT exhibited activity towards O6-G methyl groups[43].
- The concentration of overexpressed MGMT is so high that it efficiently repairs all O-6-methylguanine DNA lesions, and the only effect of TMZ we observe is due to other type of damage that MGMT is unable to repair. Testing this hypothesis would require expressing MGMT at a much lower level, which could not be done without deleting the native MGMT, or replacing it with a fluorescently-tagged variant. We attempted replacing endogenous MGMT with the MGMT-C-GFPspark construct, but could not detect the fluorescent protein in the nucleus using both wide-field and confocal microscopy, despite extensive troubleshooting.

As for the broader significance of our work, phenotypic heterogeneity in the absence of genetic changes has been proposed to be responsible for failure of some anticancer therapies[44]. Phenotypic diversity may generate resistant cells that can repopulate the tumour when sensitive cells are removed by therapy, or can provide a temporary "safe haven" for cancer cells to evolve genetic resistance – a possibility that has been suggested by others[45] and independently investigated theoretically by us[46]. However, evolutionary dynamics of non-genetic heterogeneity has not been investigated experimentally in a quantitative way that would enable one to build predictive mathematical models. Here, we attempted to quantify phenotypic heterogeneity in the response to chemotherapy and to determine how it is passed onto offspring cells. While we did not fully succeed in elucidating the mechanism of short-term response to TMZ, our results suggest that MGMT is not involved.

We also obtained quantities such as the distributions of division times, death rate, and cell motility, that could be used to construct more advanced models of glioblastoma treatment. Mathematical modelling is increasingly being used in oncology[47–49]. However, to predict cancer growth and evolution in individual patients, theoretical models must be based on experimentally verified assumptions and carefully measured parameters and their distributions in a population of cancer cells. Most published data cannot be integrated into mathematical models in this way due to different parameters measured for different cell lines, conditions, and experimental approaches. We believe that the quantitative characterization (similar to what we have attempted here) of each patient-derived cancer clone will be required to develop truly predictive models of cancer.

Materials and methods
Cell culture
U-87 MG (ECACC 89081402) cells were cultured in EMEM medium (Corning; catalogue number: 10-009-CV) supplemented with 10% foetal bovine serum (FBS) and 1% penicillin-streptomycin solution. Cells tested negative for mycoplasma contamination (Applied Biological Materials Inc, catalogue number: G238).

In preparation for live-imaging in vitro chemotherapy experiments, cells were trypsinized with 1 ml trypsin-EDTA solution for 5 min at 37 °C, and centrifuged for 5 min at 300G in EMEM medium. The supernatant was discarded and the cell pellet was resuspended in EMEM medium. 10 μl of the cell suspension was used to estimate the number of cells by an automated cell counter (BioRad TC20). Based on this, 2500 cells/well were seeded in a 24-well plate in 500 μl of EMEM medium per well. The cells were then left overnight in the incubator (Binder) at 37 °C and 5% CO_2.

Image acquisition
The 24-well plate with cell cultures was moved from the incubator to the microscope stage. Images were acquired using Nikon Eclipse Ti2-E epi-fluorescent microscope with an automated XY stage, Andor Zyla 4.2 SCMOS camera (Oxford Instruments, UK), CO_2 incubator (OKO lab), and the Perfect Focus System (Nikon), and controlled by MicroManager 2.0[50]. While imaging, the plate was incubated at 37 °C, with continuous flow of humidified air with 5% CO_2. Each well was divided into a number of overlapping fields of view (FOV) on a regular 10×10 grid, with 10% overlap between neighbouring FOVs. Table 1 shows the specific settings for each experiment. Perfect Focus System was used to adjust for the thermal drift during imaging. Images were analysed using machine learning algorithms described below.

Drug treatment
After an initial period of image acquisition, imaging was paused and plates were removed from the microscope stage. The medium was discarded and replaced with 1.5 ml fresh EMEM medium containing either 0.25% DMSO (Sigma Life Science; catalogue number: D2650-100ML) or the desired concentration of the drug temozolomide (TMZ, Sigma-Aldrich, catalogue number: T2577-25MG). The concentration of DMSO was adjusted to be the same for all conditions (control and treated populations). Non-DMSO controls were replaced with EMEM medium. Plates were put back on the microscope stage and imaging was continued. The exact time of drug addition (different for each experiment) was recorded and used in the subsequent analysis.

Experiment	Plate type and grid size	Objective	Duration	Imaging frequency/channels
Figures 1, 2 and 3; 3 replicates	Sarstedt 83.3922; 10 × 10 FOVs	20x, N.A. 0.45	Rep1: ~189 h Rep2: ~185 h Rep3: ~186.5 h	Every 10 min/BR
Figure 5; 2 replicates	Sarstedt 83.3922; 10 × 10 FOVs	20x, N.A. 0.45	~ 116 h	Every 10 min/BR Every 3 h/FITC
Figure 4; 1 replicate	Sarstedt 83.3922; 8 × 8 FOVs	20x, N.A. 0.45	~ 117 h	Every 10 min/BR Every 3 h/FITC Every 3 h/TRITC

Table 1. Imaging settings for live imaging experiments. BR = brightfield, FITC = green fluorescence filter 457.5–487.5 nm (excitation)/502.5–537.5 nm (emission), TRITC = red fluorescence filter 532–554 nm (excitation)/573–613 nm (emission).

Clonogenic assay

Cell culture dishes (60 mm) were seeded with approx. one thousand of U-87 MG cells/dish in 5 ml EMEM medium. After overnight incubation, the medium was replaced with fresh medium containing either 0.25% DMSO or the desired concentration of TMZ. The concentration of DMSO was adjusted to be the same for all conditions. Non-DMSO controls were replenished with EMEM medium. All the dishes were kept in the incubator for 2 weeks. After the incubation, the medium was replaced with 4% paraformaldehyde for 20 min to fix the cells. Cells were then washed with PBS and stained using 0.5% crystal violet solution for 20 min. After 20 min, cells were washed with water to remove excess crystal violet stain. The dishes were dried at room temperature and the number of colonies formed (visible with a naked eye) were counted manually. The experiment was performed in triplicate, each replicate starting at the end of the previous one.

Expression plasmid and transient transfection

Eukaryotic expression plasmid for human MGMT tagged with GFPspark was purchased from SinoBiological (HG12077-ACG). Fugene HD transfection reagent (Promega; catalogue number: E231 A) was used for transient transfections. 250 ng of plasmid DNA was used with the transfection reagent in a 3:1 ratio for 24-well plates. Transfection was done following the manufacturer's protocol.

Lentivirus transduction and cell cycle reporter stable cell generation

1 million U-87 MG cells in a 6-well plate were transduced with VSV-G pseudotyped Fluorescent Ubiquitination-based Cell Cycle Indicator (FUCCI)-Puro lentiviral particles (LipExoGen Biotech; catalogue number: LTV-0052–1 S) according to manufacturer's recommendation. After 48 h of lentiviral infection, cells were trypsinized and transferred to a T-25 cell culture flask with 7 ml EMEM medium. 2.5 µg/ml puromycin was added to the flask after 14–16 h of incubation. Puromycin containing EMEM medium was replaced every 48 h till the flask was 60–80% confluent. These cells were further trypsinized and seeded in a T-75 cell culture flask containing 17 ml EMEM medium with puromycin. The medium was discarded every 48 h and fresh EMEM with puromycin was added until the cells reached a confluency of 70–90% in the flask. When the desired confluency was reached, cells were trypsinized and stored for future use. Since there was no clonal amplification, the FUCCI-expressing cells obtained were polyclonal. For experiments evaluating the effect of TMZ on cell cycle, 2500 cells/well were seeded in a 24-well plate with 500 µl EMEM medium. Treatment with the drug was performed as described above.

Image and data analysis

All live-imaging experiments generated data in the form of µManager TIFF datasets. We processed these images in different ways, depending on whether the total count or individual tracks were required:

- *Image segmentation*. Individual bright-field FOVs were first stitched in ImageJ Grid/Collection Stitching plugin[51] using a custom-made script for batch processing of all FOVs from all time points. Pixel binning (2 × 2) was used to reduce image size and the run time of the algorithm. Stitched images were segmented in Cellpose 3 (version 3.0.11)[52,53] using the "cyto3" pretrained model able to deal with images of dense populations of cells (especially important for later timepoints). Processing stitched images instead of individual FOVs helped to avoid problems with segmenting cells present at the edge of adjacent FOVs. The algorithm outputted image masks, with all pixels belonging to each detected cell assigned a label unique to that cell. A visual comparison of a few segmented original and binned images showed that pixel binning did not adversely affected segmentation quality.
- *Cell number versus time*. To obtain the number of cells in each time frame, we counted the number of unique labels in the masks outputted by the above procedure.
- *Automated cell tracking*. Labelled masks of segmented images were imported into Mastodon v1.0.0-beta-34 (https://mastodon.readthedocs.io/en/latest/). Mastodon first generated spatio-temporal coordinates ("spots") (x, y, t) of each cell. Next, individual "spots" were connected into tracks using the build-in LAPtracker algorithm. The output was a collection of tracks in the Mastodon data format. A single track represented a sequence of (x, y, t) coordinates along the trajectory of a cell. Each track begun at some time t_1 when it separated from its mother cell, or at $t_1 = 0$ if the cell was present already at $t = 0$. The track ended at some time t_2 representing either (i) the next division event, (ii) cell death, (iii) the end of the experiment, (iv) the cell

disappearing from the FOV, or (v) not being traceable for other reasons. A small number of tracks that formed loops due to cells dividing but then apparently merging together were excluded from the analysis. Tracks were then imported into a Python notebook using MastodonReader version 0.3.1 (https://github.com/mastodon-sc/python-mastodon-importer) for further analysis. Many Mastodon-generated tracks had gaps due to the failure of the image segmentation algorithm. Since some of our analysis required long, uninterrupted tracks, we used a custom-made Python code to close such gaps. The algorithm followed each track backward in time and if the track suddenly ended (which was not possible biologically), the algorithm would search for nearby tracks that terminated around the same time while propagating forward in time, and connected the backward-propagating track to one of them. The selection process of new connections was a global optimization problem, in which the objective was to minimize the sum of distances between tracks' endpoints bridged by the proposed connections, plus the number of forking events (divisions), multiplied by a large number (2^{20}) to strongly penalize unnecessary connections. While this approach significantly increased the number of uninterrupted tracks, many tracks could still contain incorrectly assigned division events. For this reason, in the main text we used terms such as "branch length" instead of "division/doubling times" and "branching events" instead of "division event" to stress that the analysis was based on the structure of lineage trees and not on true division events, unless explicitly stated as in the case of manually-corrected tracks.

- *Manual cell tracking.* Stitched images were converted from TIFF to a format compatible with Mastodon v1.0.0-beta-34 (BigDataViewer format xml + h5) using a custom script. The files were opened using Mastodon launcher. Each cell was followed in time by a human operator, and its position marked every time the cell visibly moved. If the cell did not move, there would be a missing point along the track at that particular time point. In such a case, in the subsequent analysis we assumed the position was the same as the last recorded position. If a track could not be continued for reasons discussed before (cell death, cell moving out of the FOV, etc.), a special tag was assigned to it to distinguish it from tracks ending with cell death. This procedure created tracks in the same format as the automated method discussed above. For data in Fig. 4, we first created automated tracks as described above, and then manually curated them to make sure division events were correctly identified. All tracks were saved as *.mastodon files for further processing.

- *Further processing of cell tracks.* Tracks were imported into a Python notebook using MastodonReader and used to calculate motility, division times, and fluorescence as a function of time (see below). Fluorescence quantification (Figs. 4 and 5) required matching manually-created and manually-corrected tracks with segmented images of cells so that total fluorescence could be calculated for each cell at each time point. To do this, for every time frame we found the centre of mass for each Cellpose-segmented cell. Next, we identified the closest "spot" (x, y, t) in the corresponding Mastodon dataset containing cell tracks, and associated the given cell with this specific "spot". We then computed total fluorescence (see below) for the cell and appended it to the data record representing the "spot". If the distance between the cell and the "spot" was larger than 50 µm, the match was rejected and no data was added to the "spot".

Growth curves

Fold change in the number of cells was calculated as the ratio of the number of cells $N(t)$ at time t to $N(t = 0)$, where $t = 0$ corresponds to the time when TMZ was added to the plate.

Motility and division times

For each track, we calculated the instantaneous speed $v(t_i)$ from the difference in (x, y) coordinates at time t_i and t_{i+1} as $v(t_i) = \frac{\sqrt{(x_{i+1} - x_i)^2 + (y_{i+1} - y_i)^2}}{t_{i+1} - t_i}$. We then calculated the average speed of each cell as $v = (1/n) \sum_{i=1}^{n-1} v(t_i)$, and used this quantity to represent cell motility.

To obtain division times/branch lengths, we calculated the time between the consecutive division/forking events, i.e., $DT = t_n - t_1$ where t_1 and t_n are the first and last points of the track.

Fluorescence of individual cells

Uneven image illumination in wide-field fluorescent microscopy causes fluorescence to drop towards the edges of the FOV. Furthermore, background fluorescence tends to decay over time due to the medium changing its chemical composition, and photobleaching. To remove this effect, i.e., to apply flat-field correction to the image, we used BaSiC[54], a method capable of inferring the flat-field correction from a time series of images. The method can account for photobleaching and other time-dependent changes in background fluorescence. We used the multiplicative version of the method, $I_m = (B + I_t) \times F$, in which I_m is the measured intensity, I_t is the true intensity we want to obtain, B is the "baseline" signal which is pixel-independent but time-dependent, and F is the flat-field image. The algorithm solves this equation for I_t and F. Next, we used binary masks of segmented cells to compute total fluorescence of each cell.

Statistical analysis

To compare 1D distributions, we used the two-sided Kolmogorov-Smirnov test (Python SciPy 1.10.0). To compare 2D distribution, we used the 2D Kolmogorov–Smirnov test using the code written by Zhaozhou Li, https://github.com/syrte/ndtest (version 0.1) based on Refs[55,56]. Error bars represent standard errors of mean.

Mathematical model

We use an agent-based model, in which each cancer cell has four state variables: an integer "clock" $x = 1, ..., T$ representing the current position in the cell cycle, the current cell cycle stage $s = \{1, 2, 3\}$, whether the cell is methylated due to the drug $m = \{0, 1\}$, and whether the cell cycle has halted $a = \{0, 1\}$. The parameter T

represents the duration of the cell cycle as the number of discrete time intervals $dt = 30$ min. We consider three stages in the cell cycle; these could (but do not have to) represent the gap 1 (G1), synthesis (S), and gap 2 (G2) phases. We omit the M stage as the duration of this stage is very short. The phases have durations of T_1, T_2, T_3 time steps, respectively. Thus, the division time is $T = T_1 + T_2 + T_3$ time steps. The value of x increases by one every time step of the algorithm. The variable s equals 1 for $1 \leq x < T_1$, $s = 2$ for $T_1 \leq x < T_2$ and $s = 3$ for $x \geq T_2$. When the cell has reached the end of the cell cycle, $x = T$, the cell divides into two daughter cells. The two cells start at the beginning of the cell cycle ($x = 1$).

An unmethylated cell ($m = 0$) becomes methylated ($m = 1$) with rate r_{drug} (probability per unit of time) during the second phase only. Methylated cells die at the end of the third phase.

The simulation starts with N_0 unmethylated cells, with N_0 taken from the first data point of the experimental data, and with x chosen from the exponential distribution $p(x) = (2\ln2)/T\, 2^{-x/T}$. This distribution is the steady-state distribution of x, i.e., it represents a population of cells that has been growing for sufficiently long time (as in the experiment prior to the addition of TMZ) for cells to have desynchronized their cell cycles.

Fitting the model to data

We fitted the model simultaneously to all growth curves shown in Fig. 6B. All parameters were assumed to be the same for the control, 10, and 500 μM TMZ experiments, except the parameter r_{drug} which was permitted to take different values for the three conditions ($r_{\mathrm{drug=0}} = 0$ whereas $r_{\mathrm{drug=10}}, r_{\mathrm{drug=500}}$ were the fitting parameters).

Data availability

All software used for data analysis (Jupyter notebooks, Julia code), processed data and simulation results are available at https://github.com/Dioscuri-Centre/phenotypic_heterogeneity. Due to large file sizes (several TBs), access to the raw image data will be provided upon reasonable request to the corresponding author.

References

1. Tomasetti, C. & Vogelstein, B. Variation in cancer risk among tissues can be explained by the number of stem cell divisions. *Science* **347**(6217), 78–81 https://doi.org/10.1126/science.1260825 (2015).
2. Nowak, M. A. & Waclaw, B. Genes, environment, and bad luck, *Science*, **355**(6331), 1266–1267, https://doi.org/10.1126/science.aam9746 (2017).
3. Galmarini, D., Galmarini, C. M. & Galmarini, F. C. Cancer chemotherapy: A critical analysis of its 60 years of history, *Crit. Rev. Oncol. Hematol.*, **84**(2), 181–199, https://doi.org/10.1016/j.critrevonc.2012.03.002 (2012).
4. Luqmani, Y. A. Mechanisms of Drug Resistance in Cancer Chemotherapy, *Med. Princ. Pract.*, **14**(1), 35–48, https://doi.org/10.1159/000086183 (2008).
5. Mansoori, B., Mohammadi, A., Davudian, S., Shirjang, S. & Baradaran, B. The Different Mechanisms of Cancer Drug Resistance: A Brief Review, *Adv. Pharm. Bull.*, **7**(3), 339–348, https://doi.org/10.15171/apb.2017.041 (2017).
6. Klemm, F. & Joyce, J. A. Microenvironmental regulation of therapeutic response in cancer. *Trends Cell. Biol.* **25**(4), 198–213 https://doi.org/10.1016/j.tcb.2014.11.006 (2015).
7. Liotta, L. A. & Kohn, E. C. The microenvironment of the tumour–host interface. *Nature* **411**(6835), 375–379 https://doi.org/10.1038/35077241 (2001).
8. Tredan, O., Galmarini, C. M., Patel, K. & Tannock, I. F. Drug Resistance and the Solid Tumor Microenvironment, *JNCI J. Natl. Cancer Inst.*, **99**(19), 1441–1454, https://doi.org/10.1093/jnci/djm135 (2007).
9. Gerlinger, M. et al. Intratumor heterogeneity and branched evolution revealed by multiregion sequencing. *N Engl. J. Med.* **366** (10), 883–892. https://doi.org/10.1056/NEJMoa1113205 (2012).
10. Ling, S. et al., Extremely high genetic diversity in a single tumor points to prevalence of non-Darwinian cell evolution, *Proc. Natl. Acad. Sci.*, **112**, E6496–E6505, https://doi.org/10.1073/pnas.1519556112 (2015).
11. Ryser, M. D., Min, B. H., Siegmund, K. D. & Shibata, D. Spatial mutation patterns as markers of early colorectal tumor cell mobility, *Proc. Natl. Acad. Sci.*, **115**(22), 5774–5779, https://doi.org/10.1073/pnas.1716552115 (2018).
12. Sottoriva, A. et al. A Big Bang model of human colorectal tumor growth, *Nat. Genet.*, **47**(3), 209–216, https://doi.org/10.1038/ng.3214 (2015).
13. Sun, R. et al. Between-region genetic divergence reflects the mode and tempo of tumor evolution. *Nat. Genet.* **49**, 1015–1024. https://doi.org/10.1038/ng.3891 (2017).
14. Xu, X. et al. Single-Cell Exome Sequencing Reveals Single-Nucleotide Mutation Characteristics of a Kidney Tumor, *Cell*, **148**(5), 886–895, https://doi.org/10.1016/j.cell.2012.02.025 (2012).
15. Yachida, S. et al. Distant metastasis occurs late during the genetic evolution of pancreatic cancer, *Nature*, **467**(7319), 1114–1117, https://doi.org/10.1038/nature09515 (2010).
16. Raj, A. & van Oudenaarden, A. Nature, Nurture, or Chance: Stochastic Gene Expression and Its Consequences, *Cell*, **135**(2), 216–226, https://doi.org/10.1016/j.cell.2008.09.050 (2008).
17. Lund, A. H. & van Lohuizen, M. Epigenetics and cancer, *Genes Dev.*, **18**(19), 2315–2335, https://doi.org/10.1101/gad.1232504 (2004).
18. Ochs, K. & Kaina, B. Apoptosis Induced by DNA Damage O6-Methylguanine Is Bcl-2 and Caspase-9/3 Regulated and Fas/Caspase-8 Independent1, *Cancer Res.*, **60**(20), 5815–5824, (2000).
19. Sharma, S. et al. 'Role of MGMT in Tumor Development, Progression, Diagnosis, Treatment and Prognosis', *Anticancer Res.*, **29**(10), 3759–3768, (2009).
20. Esteller, M. et al. Inactivation of the DNA-Repair Gene MGMT and the Clinical Response of Gliomas to Alkylating Agents, *N. Engl. J. Med.*, **343**(19), 1350–1354, https://doi.org/10.1056/NEJM200011093431901 (2000).
21. Hermisson, M. et al. O6-methylguanine DNA methyltransferase and p53 status predict Temozolomide sensitivity in human malignant glioma cells. *J. Neurochem.* **96**(3), 766–776 https://doi.org/10.1111/j.1471-4159.2005.03583.x (2006).
22. Parker, N. R. et al. Intratumoral heterogeneity identified at the epigenetic, genetic and transcriptional level in glioblastoma, *Sci. Rep.*, **6**(1), Art. no. 1, https://doi.org/10.1038/srep22477 (2016).
23. Akgül, S. et al. Intratumoural Heterogeneity Underlies Distinct Therapy Responses and Treatment Resistance in Glioblastoma, *Cancers*, **11**, 2 https://doi.org/10.3390/cancers11020190 (2019).

24. Choi, H. J. et al. Emerging machine learning approaches to phenotyping cellular motility and morphodynamics. *Phys. Biol.* **18**(4), 041001, https://doi.org/10.1088/1478-3975/abffbe (2021).

25. Allen, M., Bjerke, M., Edlund, H., Nelander, S. & Westermark, B. Origin of the U87MG glioma cell line: Good news and bad news, *Sci. Transl. Med.*, **8**(354), 354re3, https://doi.org/10.1126/scitranslmed.aaf6853 (2016).

26. Herbener, V. J. et al. Considering the Experimental Use of Temozolomide in Glioblastoma Research, *Biomedicines*, **8**(6), 151, https://doi.org/10.3390/biomedicines8060151 (2020).

27. Beier, D. et al. Efficacy of clinically relevant Temozolomide dosing schemes in glioblastoma cancer stem cell lines. *J. Neurooncol.* **109**(1), 45–52, https://doi.org/10.1007/s11060-012-0878-4 (2012).

28. D'Atri, S. et al. Involvement of the Mismatch Repair System in Temozolomide-Induced Apoptosis, *Mol. Pharmacol.*, **54**(2), 334–341, https://doi.org/10.1124/mol.54.2.334 (1998).

29. Quiros, S., Roos, W. P. & Kaina, B. Processing of O6-methylguanine into DNA double-strand breaks requires two rounds of replication whereas apoptosis is also induced in subsequent cell cycles, *Cell Cycle*, **9**(1), 168–178, https://doi.org/10.4161/cc.9.1.10363 (2010).

30. Strobel, H. et al. Temozolomide and Other Alkylating Agents in Glioblastoma Therapy, *Biomedicines*, **7**(3), 69, https://doi.org/10.3390/biomedicines7030069 (2019).

31. Denny, B. J., Wheelhouse, R. T., Stevens, M. F. G., Tsang, L. L. H. & Slack, J. A. NMR and Molecular Modeling Investigation of the Mechanism of Activation of the Antitumor Drug Temozolomide and Its Interaction with DNA, *Biochemistry*, **33**(31), 9045–9051, https://doi.org/10.1021/bi00197a003 (1994).

32. Günther, W., Pawlak, E., Damasceno, R., Arnold, H. & Terzis, A. J. Temozolomide induces apoptosis and senescence in glioma cells cultured as multicellular spheroids, *Br. J. Cancer*, **88**(3), 463–469, https://doi.org/10.1038/sj.bjc.6600711 (2003).

33. Giese, A., Bjerkvig, R., Berens, M. E. & Westphal, M. Cost of Migration: Invasion of Malignant Gliomas and Implications for Treatment, *J. Clin. Oncol.*, **21**(8), 1624–1636, https://doi.org/10.1200/JCO.2003.05.063 (2003).

34. Gerlee, P. & Nelander, S. The Impact of Phenotypic Switching on Glioblastoma Growth and Invasion, *PLoS Comput Biol*, **8**(6), e1002556, https://doi.org/10.1371/journal.pcbi.1002556 (2012).

35. Evdokimova, V., Tognon, C., Ng, T. & Sorensen, P. H. B. Reduced proliferation and enhanced migration: Two sides of the same coin? Molecular mechanisms of metastatic progression by YB-1, *Cell Cycle*, **8**(18), 2901–2906, https://doi.org/10.4161/cc.8.18.9537 (2009).

36. Sakaue-Sawano, A. et al. Genetically Encoded Tools for Optical Dissection of the Mammalian Cell Cycle. *Mol. Cell.* **68**(3), 626–640 https://doi.org/10.1016/j.molcel.2017.10.001 (2017).

37. Wang, T., Pickard, A. J. & Gallo, J. M. Histone methylation by temozolomide; A classic DNA methylating anticancer drug. *Anticancer Res.* **36**(7), 3289–3299 (2016).

38. De Hauwer, C. et al. Dynamic Characterization of Glioblastoma Cell Motility, *Biochem. Biophys. Res. Commun.*, **232**(2), 267–272, https://doi.org/10.1006/bbrc.1997.6291 (1997).

39. Parker, J. J. et al. Intratumoral heterogeneity of endogenous tumor cell invasive behavior in human glioblastoma. *Sci. Rep.* **8**(1), 18002, https://doi.org/10.1038/s41598-018-36280-9 (2018).

40. Erasimus, H., Gobin, M., Niclou, S. & Van Dyck, E. DNA repair mechanisms and their clinical impact in glioblastoma. *Mutat. Res. Rev. Mutat. Res.* **769**, 19–35, https://doi.org/10.1016/j.mrrev.2016.05.005 (2016).

41. Montaldi, A. P., Godoy, P. R. D. V. & Sakamoto-Hojo, E. T. APE1/REF-1 down-regulation enhances the cytotoxic effects of temozolomide in a resistant glioblastoma cell line, *Mutat. Res. Toxicol. Environ. Mutagen.*, **793**, 19–29, https://doi.org/10.1016/j.mrgentox.2015.06.001 (2015).

42. Yi, G. Z. et al. Acquired temozolomide resistance in MGMT-deficient glioblastoma cells is associated with regulation of DNA repair by DHC2, *Brain J. Neurol.*, **142**(8), 2352–2366, https://doi.org/10.1093/brain/awz202 (2019).

43. Murawska, G. M. et al. Repurposing the damage repair protein Methyl guanine Methyl transferase as a ligand inducible fusion Degron. *ACS Chem. Biol.* **17**(1), 24–31, https://doi.org/10.1021/acschembio.1c00771 (2022).

44. Brock, A., Chang, H. & Huang, S. Non-genetic heterogeneity — a mutation-independent driving force for the somatic evolution of tumours. *Nat. Rev. Genet.* **10**(5), 336–342, https://doi.org/10.1038/nrg2556 (2009).

45. Sharma, S. V. et al. A Chromatin-Mediated Reversible Drug-Tolerant State in Cancer Cell Subpopulations, *Cell*, **141**(1), 69–80, https://doi.org/10.1016/j.cell.2010.02.027 (2010).

46. Tadrowski, A. C., Evans, M. R. & Waclaw, B. Phenotypic switching can speed up microbial evolution. *Sci. Rep.* **8**(1), 8941, https://doi.org/10.1038/s41598-018-27095-9 (2018).

47. Barbolosi, D., Ciccolini, J., Lacarelle, B., Barlési, F. & André, N. Computational oncology — mathematical modelling of drug regimens for precision medicine, *Nat. Rev. Clin. Oncol.*, **13**(4), 242–254, https://doi.org/10.1038/nrclinonc.2015.204 (2015).

48. West, J. et al. A survey of open questions in adaptive therapy: Bridging mathematics and clinical translation, *eLife*, **12**, e84263, https://doi.org/10.7554/eLife.84263 (2023).

49. Enderling, H., Alfonso, J. C. L., Moros, E., Caudell, J. J. & Harrison, L. B. Integrating Mathematical Modeling into the Roadmap for Personalized Adaptive Radiation Therapy, *Trends Cancer*, **5**(8), 467–474, https://doi.org/10.1016/j.trecan.2019.06.006 (2019).

50. Edelstein, A. D. et al. Advanced methods of microscope control using MManager software. *J. Biol. Methods.* **1** (2), e10. https://doi.org/10.14440/jbm.2014.36 (2014).

51. Preibisch, S., Saalfeld, S. & Tomancak, P. Globally optimal stitching of tiled 3D microscopic image acquisitions, *Bioinformatics*, **25**(1)1, 1463–1465, https://doi.org/10.1093/bioinformatics/btp184 (2009).

52. Stringer, C., Wang, T., Michaelos, M. & Pachitariu, M. Cellpose: a generalist algorithm for cellular segmentation, *Nat. Methods*, **18**(1), 100–106, https://doi.org/10.1038/s41592-020-01018-x (2021).

53. Stringer, C. & Pachitariu, M. Cellpose3: one-click image restoration for improved cellular segmentation, Feb. 25, *bioRxiv* (2024). https://doi.org/10.1101/2024.02.10.579780

54. Peng, T. et al. A basic tool for background and shading correction of optical microscopy images. *Nat. Commun.* **8**(1), 14836, https://doi.org/10.1038/ncomms14836 (2017).

55. Peacock, J. A. Two-dimensional goodness-of-fit testing in astronomy. *Mon not R Astron. Soc.* **202**, 615–627, https://doi.org/10.1093/mnras/202.3.615 (1983).

56. Fasano, G. & Franceschini, A. A multidimensional version of the Kolmogorov-Smirnov test. *Mon not R Astron. Soc.* **225**, 155–170, https://doi.org/10.1093/mnras/225.1.155 (1987).

Acknowledgements

Author contributions

B.W. and P.D. conceived the research. P.D. and I. D.-C. carried out experiments. I. D.-C., B.W., K.D., and P.D. analysed the data. S.S., B.W. and A.T. conceived the mathematical model. S.S. wrote the code, run simulations and fitted them to the experimental data. B.W. wrote the manuscript with inputs from all authors. All authors

read and approved the final manuscript.

Declarations

Competing interests
The authors declare no competing interests.

Additional information
Supplementary Information The online version contains supplementary material available at https://doi.org/10.1038/s41598-025-99426-6.

Correspondence and requests for materials should be addressed to B.W.

Reprints and permissions information is available at www.nature.com/reprints.

Publisher's note Springer Nature remains neutral with regard to jurisdictional claims in published maps and institutional affiliations.